

Deconvolution of multiple images with high dynamic range and an application to LBT LINC-NIRVANA

B. Anconelli¹, M. Bertero¹, P. Boccacci¹, G. Desiderà¹, M. Carillet², and H. Lanteri²

¹ DISI, Università di Genova, via Dodecaneso 35, 16146 Genova, Italy
e-mail: bertero@disi.unige.it

² Laboratoire Universitaire d'Astrophysique de Nice, UMR 6525, Parc Valrose, 06108 Nice Cedex 02, France

Received 15 June 2006 / Accepted 6 September 2006

ABSTRACT

Context. The standard Richardson-Lucy method (RLM) does not work well in the deconvolution of astronomical images containing objects with very different angular scales and magnitudes. Therefore, modifications of RLM, applicable to this kind of objects, must be investigated.

Aims. We recently proposed a regularization of RLM which provides satisfactory results in the case of particular test objects with high dynamic range. In this paper we extend this method to the case of multiple image deconvolution, having in mind application to the reconstruction of the images provided by Fizeau interferometers such as LINC-NIRVANA, the German-Italian beam combiner for the Large Binocular Telescope.

Methods. RLM is an iterative method for the minimization of the Csiszár divergence, a problem equivalent to maximum likelihood estimation in the case of photon noise. In our approach, the problem is regularized by adding a suitable penalization term to the Csiszár divergence and an iterative method converging to the minimum of the resulting functional is derived from the so-called split gradient method (SGM).

Results. The method is tested on a model of young binary star consisting of a core binary surrounded by a dusty circumbinary ring. The results are quite good in the case of exact knowledge of the point spread functions (PSF). However, in the case of approximate knowledge of the PSFs, the accuracy of the reconstruction depends on the difference of magnitude between the ring and the central binary.

Key words. methods: numerical – techniques: image processing

1. Introduction

In previous papers (Bertero & Boccacci 2000a,b; Correia et al. 2002; Carillet et al. 2002; Anconelli et al. 2005) we developed methods and software for the deconvolution of multiple interferometric images of the same astronomical target. One of the results is the software package AIRY (Astronomical Image Reconstruction in interferometry) of which version 3.0 is now available (see <http://dirac.disi.unige.it> and <http://www-luan.unice.fr/caos>). This tool, described in Correia et al. (2002), can be applied to Fizeau interferometers such as LINC-NIRVANA (Lbt INterferometric Camera and Near-InfraRed/Visible Adaptive iNterferometer for Astronomy), in the following denoted by LN, the German-Italian beam combiner for the Large Binocular Telescope (LBT). LBT, under completion on Mount Graham, Arizona, will consist of two 8.4 m mirrors on a common mount, with a spacing of 14.4 m between their centres, so that a maximum baseline of 22.8 m will be available. The two primary mirrors have been already installed and aluminized; “first light” has been achieved on October 12, 2005.

The methods we have implemented and validated are, essentially, accelerated versions of the multiple-image Richardson-Lucy method (RLM), in particular the so-called ordered subset expectation maximization (OSEM) method. As it is known both RLM and OSEM need an early stopping of the iterations in order to avoid the so-called *checkerboard effect* in the case

of diffuse objects. Moreover, in the case of a field containing both diffuse and pointwise objects, providing different signal-to-noise ratios (SNR) in different regions of the image domain, both RLM and OSEM have different convergence rates in these different regions. One can try to overcome this difficulty by some kind of explicit *adaptive regularization*, acting in a different way on diffuse and pointwise objects.

Methods with such a property have been already proposed and investigated. For a recent review see Puetter et al. (2005). In this paper we attack the problem with another method, based on a suitable global regularization, which can be easily implemented and can work well in the case of scientific targets satisfying the following conditions:

- the object consists of very bright stars and of faint diffuse structures so that there exists a wide gap between their intensities;
- there exists an angular separation between the two kinds of objects, i.e. they are located in different regions of the field of view (FOV).

An example of such an object is shown in Fig. 1. It is a model of young binary star surrounded by a dusty circumbinary ring, described in Carillet et al. (2002). It is directly inspired by near-infrared observations of the T-Tauri binary star of the quadruple system GG Tau and subsequent modeling by Wood et al. (1999). The main features of the model are the following: the object is an array 256×256 , so that, with a pixel size corresponding to

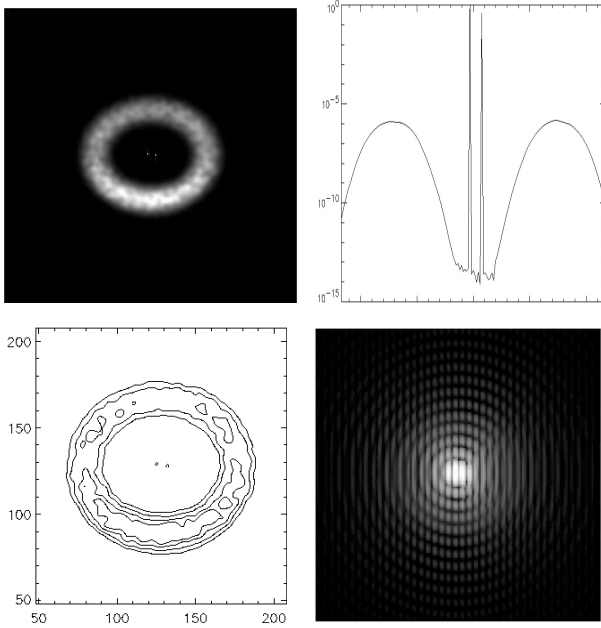


Fig. 1. *Upper-left panel:* gray level representation of the model of young binary star described in the text. *Upper-right panel:* the cut of the object (normalized to unit maximum value) along the direction of the binary system. *Lower-left panel:* representation of the ring by means of level curves (corresponding to the values 2460, 4320, 7020, and 9720; the maximum value of the ring is 1.45×10^4 , while the maximum value of the binary is 5.39×10^9). *Lower-right panel:* gray level representation, in a log-scale, of the image corresponding to an ideal PSF of LN, with 0° relative parallactic angle.

that of the LN detector (5.12 mas), it has an extension of about 1.31 arcsec; it is observed in K band and has a total magnitude of 9.63; the integrated magnitude of the ring is 15.25 while the magnitudes of the two stars are 10 and 11, respectively. Moreover, the angular separation of the binary is about twice the angular resolution of LN in K band (20 mas). The cut of the object (normalized to unit maximum value) along the direction of the binary star is plotted in the upper-right panel of Fig. 1, to show that there is about a factor 10^6 between the flux of the primary and the average flux of the ring. The structure of the ring is shown in the lower-left panel by means of a representation in terms of level curves. It is obvious that, in such a situation, the side lobes of the images of the two stars are superimposed to the ring and mask its structure. This effect is illustrated in the lower-right panel of the same figure where we give the image obtained by convolving the object with an ideal interferometric PSF of LN. This object will be used in our numerical simulations.

Our approach will be based on a regularization functional containing a *thresholding parameter*, assuring that the reconstruction of the bright point objects above the value of the parameter is not regularized, while the reconstruction of the faint objects, below the value of the parameter is regularized in a *Tikhonov-like* manner (see, for instance, Bertero & Boccacci 1998). Therefore it contains also a *Tikhonov regularization parameter*, which must be optimized.

This approach has been recently proposed in the case of single image deconvolution (Anconelli et al. 2006b) and, in this paper, it will be extended to the problem of multiple image deconvolution in view of its application to the reconstruction of LN interferometric images. In Sect. 2 we discuss the functional we propose for the regularization of the maximum likelihood approach in the case of photon noise, by comparing its effect

with that of the standard Tikhonov functional. In Sect. 3 we derive modified versions of RLM and OSEM able to minimize the regularized functional. In Sect. 4 we present our numerical experiments based on the test object of Fig. 1, using both ideal and AO corrected PSFs. Finally in Sect. 5 we discuss the limitations of our approach.

2. The regularized functional

We use bold letters for denoting $N \times N$ arrays, whose pixels are indexed by a multi-index $\mathbf{n} = \{n_1, n_2\}$. Moreover, we assume that we have p images acquired with LN, corresponding to p different orientations of the baseline and denoted by $\mathbf{g}_1, \mathbf{g}_2, \dots, \mathbf{g}_p$. If $g_j(\mathbf{n})$ is the value of the j th image at pixel \mathbf{n} , then, according to the model proposed by Snyder et al. (1993) for data acquired with a CCD camera, we can write:

$$\mathbf{g}_j(\mathbf{n}) = \mathbf{g}_{\text{obj},j}(\mathbf{n}) + \mathbf{g}_{\text{back},j}(\mathbf{n}) + \mathbf{r}_j(\mathbf{n}), \quad (1)$$

where: $\mathbf{g}_{\text{obj},j}(\mathbf{n})$ is the number of photoelectrons due to radiation from the object; $\mathbf{g}_{\text{back},j}(\mathbf{n})$ is the number of photoelectrons due to external and internal background, dark current, etc.; $\mathbf{r}_j(\mathbf{n})$ is the read-out noise due to the amplifier. The first two terms are realizations of independent Poisson processes (photon noise), so that their sum is also a Poisson process; its expected value is given by:

$$E\{\mathbf{g}_{\text{obj},j}(\mathbf{n}) + \mathbf{g}_{\text{back},j}(\mathbf{n})\} = (\mathbf{K}_j * \mathbf{f})(\mathbf{n}) + \mathbf{b}_j, \quad (2)$$

where: \mathbf{K}_j is the PSF corresponding to the j th orientation of the baseline; \mathbf{f} is the object array; \mathbf{b}_j is the (constant) expected value of the background. We assume, as usual, that the PSFs are normalized to one:

$$\sum_{\mathbf{n}} \mathbf{K}_j(\mathbf{n}) = 1. \quad (3)$$

If the images are dominated by photon noise, as in the cases we are considering, the read-out noise can be neglected, and the likelihood function is given by a product of Poisson distributions, one for each pixel of the image domain. The maximization of this function is equivalent to the minimization of the Csiszár divergence (Csiszár 1991) given by:

$$J(\mathbf{f}; \mathbf{g}) = \sum_{j=1}^p \sum_{\mathbf{n}} \{g_j(\mathbf{n}) \ln \frac{g_j(\mathbf{n})}{(A_j \mathbf{f})(\mathbf{n}) + \mathbf{b}_j} + [(A_j \mathbf{f})(\mathbf{n}) + \mathbf{b}_j - g_j(\mathbf{n})]\}, \quad (4)$$

where \mathbf{g} denotes the set of the p images \mathbf{g}_j and A_j is the matrix defined by:

$$A_j \mathbf{f} = \mathbf{K}_j * \mathbf{f}. \quad (5)$$

Multiple-image RLM and OSEM (Bertero & Boccacci 2000b) are just iterative methods for the minimization of this functional.

Regularization of the Csiszár divergence can be achieved by adding a suitable penalty term and the problem becomes the minimization of functionals of the following form:

$$J_\mu(\mathbf{f}; \mathbf{g}) = J(\mathbf{f}; \mathbf{g}) + \mu J_R(\mathbf{f}), \quad (6)$$

where μ is the regularization parameter.

The standard Tikhonov regularization, can be obtained by taking:

$$J_R(\mathbf{f}) = \|\mathbf{f}\|^2 = \sum_{\mathbf{n}} |\mathbf{f}(\mathbf{n})|^2. \quad (7)$$

However, in the case of bright point objects combined with diffuse faint objects, this functional is dominated by the point objects and is not significantly affected by the faint ones. For instance, in the case of the object of Fig. 1, the value of this functional is 3.36×10^{19} . Since the brightness of the primary component of the binary is 5.39×10^9 while the brightness of the secondary component is 2.14×10^9 , we find that the ring contributes to the fourth digit of the value of this functional. Therefore it is obvious that such a functional regularizes the binary but does not regularize the faint ring.

This effect can be removed if it is possible to “mask” in some way the bright point objects. This goal can be achieved by a very simple modification of the previous functional, already investigated in Anconelli et al. (2006b):

$$J_R(\mathbf{f}) = \eta^2 \sum_{\mathbf{n}} \frac{|\mathbf{f}(\mathbf{n})|^2}{|\mathbf{f}(\mathbf{n})|^2 + \eta^2}. \quad (8)$$

Indeed this functional is constant (no penalty) in the regions where the brightness of the object is much greater than η , while it provides a Tikhonov-like penalty in the regions where the brightness is much smaller than η ; moreover this penalty is smoothly varying when the brightness increases.

We recall that this functional was first proposed for edge-preserving regularization (hence with the object values replaced by the values of the modulus of the gradient) by Geman & Mc Clure (1987). We also point out that the function defined in Eq. (8) is not convex, but quasi-convex, i.e. all its sub-level sets are convex, and that it has a unique global minimum at $\mathbf{f} = 0$.

3. The iterative algorithm

An iterative method for the minimization of the functional defined by Eqs. (6), (4), and (8), with the additional constraints of non-negativity and flux conservation:

$$\mathbf{f}(\mathbf{n}) \geq 0, \quad (9)$$

$$\sum_{\mathbf{n}} \mathbf{f}(\mathbf{n}) = \frac{1}{p} \sum_{j=1}^p \sum_{\mathbf{n}} \{\mathbf{g}_j(\mathbf{n}) - \mathbf{b}_j\} \doteq c,$$

can be obtained by means of a general approach known as split gradient method (SGM), proposed by Lanteri et al. (2001, 2002). The extension of this approach to the problem of multiple image deconvolution is discussed in Anconelli et al. (2004). The method provides iterative algorithms that, in general, are not very efficient (they require a large number of iterations) but have a very nice feature: for very broad classes of regularization functionals they can be obtained by means of a very simple modification of RLM or OSEM and therefore can be easily implemented by everybody. In such a way it is easy to compare the results obtainable by means of different regularization functionals. In particular we will apply the method to the case of the two regularization functionals given by Eqs. (7) and (8) respectively. Of course, once a specific regularized functional has been selected for the specific problem at hand, one can use more efficient optimization methods for its minimization.

The basic point is the following decomposition of the gradient of the functional of Eq. (6):

$$-\nabla_{\mathbf{f}} J_{\mu}(\mathbf{f}; \mathbf{g}) = \mathbf{U}_{\mu}(\mathbf{f}; \mathbf{g}) - \mathbf{V}_{\mu}(\mathbf{f}; \mathbf{g}), \quad (10)$$

where $\mathbf{U}_{\mu}(\mathbf{f}; \mathbf{g})$ and $\mathbf{V}_{\mu}(\mathbf{f}; \mathbf{g})$ are positive arrays depending on \mathbf{f} and \mathbf{g} . Then SGM can be obtained by applying the method of successive approximations to the fixed point equation derived

from the Kuhn-Tucker conditions. A discussion is contained in a recently published paper (Anconelli et al. 2006a). As a result, the general structure of the iterative algorithm is the following:

$$\mathbf{f}^{(k+1)} = \mathbf{f}^{(k)} \frac{\mathbf{U}_{\mu}(\mathbf{f}^{(k)}; \mathbf{g})}{\mathbf{V}_{\mu}(\mathbf{f}^{(k)}; \mathbf{g})}. \quad (11)$$

The convergence of this algorithm has not been proved in general, but only in some particular cases; nevertheless it has been verified experimentally in all the applications we have considered. An interesting feature of this algorithm is that non-negativity of the iterates is automatically satisfied, as one can easily verify.

Now, by computing the gradient of the regularized functional, we find that we can write:

$$\mathbf{U}_{\mu}(\mathbf{f}; \mathbf{g}) = \sum_{j=1}^p A_j^T \frac{\mathbf{g}_j}{A_j \mathbf{f} + \mathbf{b}_j} + \mu \mathbf{U}_R(\mathbf{f}), \quad (12)$$

$$\mathbf{V}_{\mu}(\mathbf{f}; \mathbf{g}) = p \mathbf{1} + \mu \mathbf{V}_R(\mathbf{f}),$$

where $\mathbf{1}$ is the array whose entries are all equal to 1, and $\mathbf{U}_R(\mathbf{f})$, $\mathbf{V}_R(\mathbf{f})$ are the arrays from the decomposition of the gradient of $J_R(\mathbf{f})$. Then, from Eq. (11) we obtain the following modification of the multiple-image RLM algorithm:

$$\mathbf{f}^{(k+1)} = \frac{\mathbf{f}^{(k)}}{p \mathbf{1} + \mu \mathbf{V}_R(\mathbf{f}^{(k)})} \times \left(\sum_{j=1}^p A_j^T \frac{\mathbf{g}_j}{A_j \mathbf{f}^{(k)} + \mathbf{b}_j} + \mu \mathbf{U}_R(\mathbf{f}^{(k)}) \right), \quad (13)$$

which is the general structure of a regularized multiple-image RLM.

In the particular case of the regularization functional of Eq. (7), by taking into account that we are considering the restriction of this functional to the cone of the non-negative arrays, we can choose the following decomposition of its gradient:

$$\mathbf{U}_R(\mathbf{f}) = 0, \quad \mathbf{V}_R(\mathbf{f}) = 2\mathbf{f}; \quad (14)$$

analogously, in the case of the functional of Eq. (8), we can choose the decomposition:

$$\mathbf{U}_R(\mathbf{f}) = 0, \quad \mathbf{V}_R(\mathbf{f}) = \frac{2\eta^4 \mathbf{f}}{(\mathbf{f}^2 + \eta^2)^2}. \quad (15)$$

Therefore, by looking at Eq. (13), we find that, in both cases, the modification of the RLM algorithm consists uniquely in the insertion of a multiplicative factor in the r.h.s. The OS-version of this algorithm, including also the constraint on the total flux, as deduced from the general form derived in Anconelli et al. (2004), is the following:

- choose an initial $\mathbf{f}^{(0)}$ satisfying the constraints (9);
- given $\mathbf{f}^{(k)}$, set $j = (k + 1) \bmod p$ and compute:

$$\tilde{\mathbf{f}}^{(k+1)} = \frac{\mathbf{f}^{(k)}}{\mathbf{1} + \frac{\mu}{p} \mathbf{V}_R(\mathbf{f}^{(k)})} A_j^T \frac{\mathbf{g}_j}{A_j \mathbf{f}^{(k)} + \mathbf{b}_j}, \quad (16)$$

$$\tilde{c}^{(k+1)} = \sum_{\mathbf{n}} \tilde{\mathbf{f}}^{(k+1)}(\mathbf{n});$$

- set:

$$\mathbf{f}^{(k+1)} = \frac{c}{\tilde{c}^{(k+1)}} \tilde{\mathbf{f}}^{(k+1)}. \quad (17)$$

If $\mu = 0$ this algorithm is precisely the OSEM method as given, for instance, in Anconelli et al. (2005). Moreover, if $\mu \neq 0$ and $V_R(\mathbf{f})$ is given by Eq. (14), the algorithm will be called TKR (Tikhonov Regularization) algorithm while it will be called HDR (High Dynamic Regularization) algorithm if $V_R(\mathbf{f})$ is given by Eq. (15). In this case it is easy to verify that, if, in one pixel, the value of $f^{(k)}$ is large with respect to η , then, in that pixel, we have a standard OSEM iteration; on the other hand, if the value of $f^{(k)}$ is small with respect to η , then we have, in that pixel, a TKR iteration.

4. Numerical results

The regularization methods described in the previous sections have been validated by means of numerical simulations in the case of the test object shown in Fig. 1.

In a first set of experiments we used the same PSFs for convolving the object and deconvolving the images. This is the so-called *inverse crime* and is investigated for establishing the best performance achievable with the proposed HDR algorithm. For completeness we compared the results with those provided by the TKR algorithm (Tikhonov regularization). However it is expected that a poor knowledge of the PSFs can significantly degrade the quality of the results, as a consequence of the high ratio between the brightness of the stars and that of the ring. We will verify that this is the case, indeed. Therefore, in a second set of experiments we will use PSFs with different Strehl ratio (*SR*) for convolving the object and deconvolving the images and we will find that a reliable reconstruction can be obtained only in the case of an object where the difference of magnitude between the ring and the binary is decreased.

4.1. Exact PSFs: *inverse crime*

We investigate the case of LN observations by assuming that three different images are obtained with three different orientations of the baseline, corresponding to relative parallactic angles of 0° , 60° and 120° . Moreover, in order to investigate the effect of partial AO-correction, we use three different sets of PSFs: the first consists of ideal PSFs while the second and third set consist of AO-corrected PSFs with very different values of *SR*, i.e. 70% and 26%, respectively. These PSFs are already described and used for numerical simulations in Anconelli et al. (2004, 2005). The 256×256 images are formed by convolving the model with the PSFs of a given set. Sky background emission in *K* band ($12.5 \text{ mag/arcsec}^2$) is added to the results, which are also perturbed with Poisson and Gaussian ($10 \text{ e}^- \text{ rms}$) noise. For image generation the following parameters are used: a total efficiency of 25%, an integration time of 20 min and a telescope surface of 104 m^2 .

Since images are dominated by photon noise, the variation of the SNR over the FOV can be estimated by remarking that, in the region of the binary, the peak value of the images is of the order of 10^8 , while, in the region of the ring is of the order of 10^5 . This large peak value is due to contribution from the image of the binary, since, in the object, the maximum value of the ring is of the order of 10^4 .

As already discussed in the Introduction, our regularization functional contains a thresholding parameter η , related to the intensity gap between bright and faint objects. This parameter, however, can not be directly estimated from the detected images and therefore our approach requires two steps: the first is a reconstruction based on standard OSEM, which is used for estimating η ; the second is the reconstruction based on the HDR

algorithm, including an optimization of the value of the regularization parameter μ .

Before discussing the results of our simulations, we must introduce some figures of merit (FOM) for quantifying the quality of the reconstructions. For the ring we can use the relative rms defined by:

$$\rho_{\text{rel}}^{(k)} = \frac{\|\mathbf{f}_{\text{ring}}^{(k)} - \mathbf{f}_{\text{ring}}\|}{\|\mathbf{f}_{\text{ring}}\|}, \quad (18)$$

where \mathbf{f}_{ring} is the array obtained by masking the binary in the original object while $\mathbf{f}_{\text{ring}}^{(k)}$ is the array obtained in the same way from the result of the k th iteration of the iterative method one is considering.

Moreover, for checking the accuracy in the reconstruction of the photometry of the binary, we can compute, at each iteration, the fluxes of the two stars, by using 3×3 arrays centered on their positions. In such a way it is also possible to compute their magnitudes and their difference of magnitudes.

Finally, to check the statistical goodness of the reconstructions, we looked at the normalized residuals of the solutions, defined by:

$$\mathbf{R}_j(\mathbf{n}) = \frac{g_j(\mathbf{n}) - [(A_j \mathbf{f})(\mathbf{n}) + \mathbf{b}_j]}{\sqrt{(A_j \mathbf{f})(\mathbf{n}) + \mathbf{b}_j}}, \quad j = 1, \dots, p. \quad (19)$$

If $A_j \mathbf{f} + \mathbf{b}_j$ is the exact model corresponding to the images g_j , then the corresponding residual is essentially a realization of white noise. On the other hand, if \mathbf{f} is the reconstructed image and is free of artifacts, then the corresponding residual should have a similar behaviour, otherwise it will exhibit spatial correlations (see Puetter et al. 2005, for a discussion).

About the estimate of the thresholding parameter η , we checked that after 400 iterations, OSEM provides a satisfactory estimate of the maximum value of the ring, that is about 1.5×10^4 . Therefore we expect η to be greater than this value. We have found that this is the correct condition because, when it is satisfied, the results provided by the HDR algorithm do not depend on the particular value of η . All our computations have been done by taking $\eta = 4.5 \times 10^4$.

The next point is to understand where to search for the best value of the regularization parameter μ . This problem arises both in the case of TKR and in the case of HDR algorithm. In both cases one can guess that the best choice is that providing a balance between the two terms of the regularized functional of Eq. (6) when the reconstructed object is close to the exact model \mathbf{f} . Therefore we computed the value of the first term in Eq. (6) for the three sets of PSFs and we found values ranging from 9.84×10^4 to 9.94×10^4 , values very close to the expected value of this functional, namely $p N^2/2 = 9.83 \times 10^4$. Since the value of the functional of Eq. (7) is 3.36×10^{19} , we can guess that, in the case of TKR algorithm, we should have $\mu \approx 3 \times 10^{-15}$. On the other hand, the value of the functional of Eq. (8), with $\eta = 4.5 \times 10^4$, is 2.88×10^{11} , so that we guess that for the HDR algorithm we should have $\mu \approx 3 \times 10^{-7}$. A rough search for the best values of the regularization parameters in a region around the previously estimated values has demonstrated that they work surprisingly well and that they can be used to get the best reconstructions achievable by means of the two methods.

In Fig. 2 (upper panel) we plot the behaviour of the relative rms error, $\rho_{\text{rel}}^{(k)}$, defined in Eq. (18), as a function of the number of iterations k , in the case of OSEM, TKR and HDR algorithms (ideal PSFs). It is evident that both OSEM and TKR have a minimum of the reconstruction error (semiconvergence of the

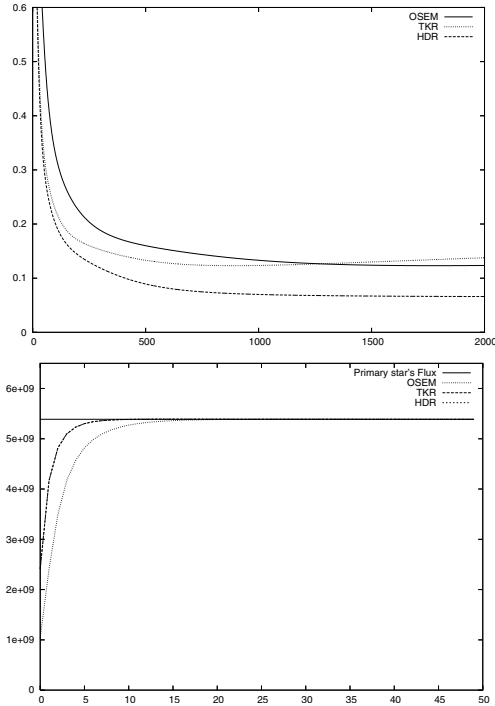


Fig. 2. *Upper panel:* the relative rms error in the reconstruction of the ring as a function of the number of iterations in the case of OSEM (full line), TKR (dotted line) and HDR (dashed line); ideal PSFs are assumed. *Lower panel:* behaviour of the flux of the primary star as a function of the number of iterations in the same cases of the upper panel.

Table 1. Values of the rms error in the reconstruction of the ring: in the case of OSEM and TKR we give the minimum values and, in brackets, the corresponding number of iterations; in the case of HDR we give the limiting values, which are reached after a number of iterations of the order of 2000. The values of the parameters η and μ are those indicated in the text.

	Ideal	AO 70%	AO 26%
OSEM	12.3 (1770)	20.4 (4150)	58.2 (10670)
TKR	12.3 (886)	20.8 (2110)	62.6 (5330)
HDR	6.5	9.3	28.4

method) while HDR is convergent. We point out that OSEM and TKR provide the same value of the minimum rms (the only difference is that TKR is a bit faster), while the minimum rms provided by HDR is considerably smaller.

In Table 1 we give the minimum values of the rms obtained by applying the three algorithms (in brackets the number of iterations required for reaching the minimum). We point out that both the reconstruction error and the number of iterations increase with decreasing SR .

In the lower panel of Fig. 2, we plot the behaviour of the flux of the primary star as a function of the number of iterations, for the three cases considered in the upper panel. The convergence is very fast and is faster for the regularized methods; we obtain a 9% error after 10 iteration and a 1% error after 50 iterations. However this accuracy concerns the photometry, as computed in the way indicated above, and not the pointwise structure of the binary, as we can see by looking at the residuals

These are shown in Fig. 3 both in the case of the exact object and in the case of the reconstructions corresponding to the minimum rms error on the ring. It is evident that the residual corresponding to the reconstruction provided by the

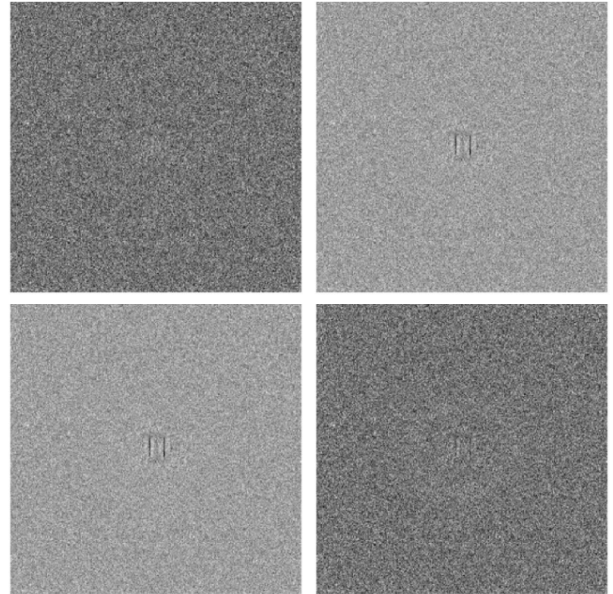


Fig. 3. Residuals corresponding to the original object and to the reconstructed images obtained by the different methods. *Upper-left panel:* the exact object. *Upper-right panel:* the OSEM reconstruction. *Lower-left panel:* the TKR reconstruction. *Lower-right panel:* the HDR reconstruction.

HDR algorithm is free of artifacts while those corresponding to the solutions provided by OSEM and TKR algorithms show artifacts in the central region indicating, as expected, that the reconstruction of the binary is not completely satisfactory.

We also checked the behaviour of the χ^2 function. Since in each pixel of our images we have a very large number of photons, we use the following simplified form of the unbiased χ^2_γ function introduced by Mighell (1999):

$$\bar{\chi}^2_\gamma = \frac{1}{pN^2} \sum_{j=1}^p \sum_n \frac{|g_j(\mathbf{n}) + 1 - [(A_j f)(\mathbf{n}) + \mathbf{b}_j]|^2}{g_j(\mathbf{n}) + 1}. \quad (20)$$

In all cases of Table 1 this quantity is decreasing and tending to 1 as the number of iterations increases. However, if we consider, for instance, the case of ideal PSFs, for OSEM and TKR, the $\bar{\chi}^2$ takes the value 1.04 in correspondence of the minimum rms error in the reconstruction of the ring. If we increase the number of iterations, then this quantity decreases but the reconstruction of the ring is considerably degraded. On the other hand, in the case of HDR, the $\bar{\chi}^2$ takes the value 1.01 after 2000 iterations and still decreases for a larger number of iterations while the reconstruction of the ring remains stable. We think that these results confirm the statistical significance of our approach.

The quality of the reconstructions of the ring can also be appreciated by looking at the reconstruction of the level curves shown in Fig. 1 (lower-left panel). Therefore, in Fig. 4 we compare the reconstructions of these level curves, as provided by OSEM and by the HDR algorithm, while we do not show those provided by the TKR algorithm because they look very similar to the OSEM reconstructions. We give all the results we have obtained using both ideal and AO-corrected PSFs. We see that the quality of the reconstruction decreases for decreasing values of the SR .

Finally, we also considered FOMs defined as the ratio between the flux of the main star and the flux of regions of the ring. To this purpose we considered two domains, each 10×5 pixels,

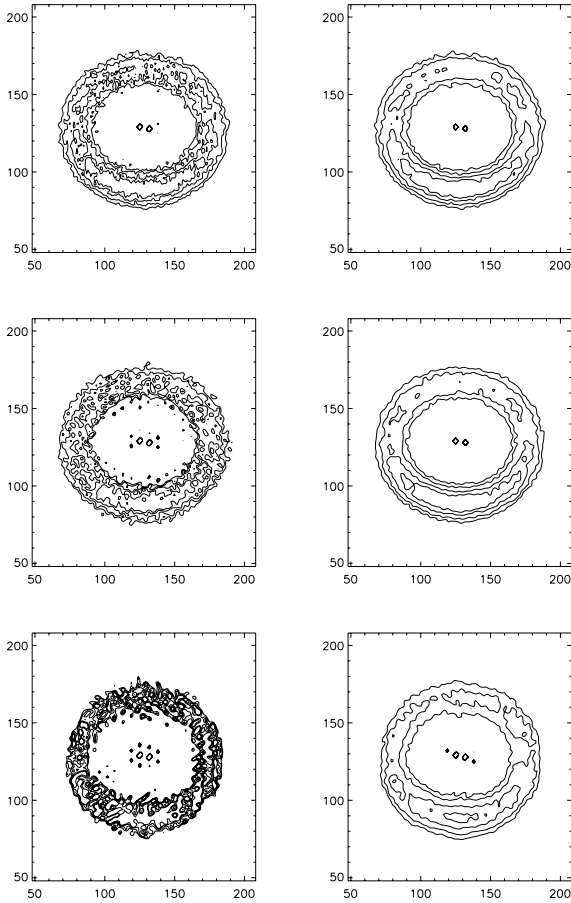


Fig. 4. Reconstruction of the level curves of the ring corresponding to the values indicated in Fig. 1. In the *left column* we display the best reconstructions provided by OSEM and in the *right column* those provided by the HDR algorithm. *From top to bottom*: ideal PSFs, AO-corrected PSFs with $SR = 70\%$ and AO-corrected PSFs with $SR = 26\%$.

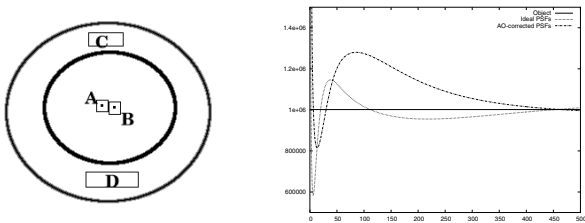


Fig. 5. *Left panel*: picture of the different areas of the ring where we check the accuracy of the restoration. *Right panel*: behaviour of the ratio between the areas A and C as a function of the number of iterations both in the case of ideal PSFs and in the case of AO-corrected PSFs ($SR \approx 70\%$).

one on the front and the other on the back of the ring. These areas are shown in the left panel of Fig. 5. In the right panel of the same figure we plot, as a function of the number of iterations, the ratio between the flux of A and that of C. The correct value is reached after a few hundreds of iterations in the case of both ideal and AO-corrected PSFs.

4.2. Approximate PSFs

The previous results are quite promising but they are based on the assumption of an exact knowledge of the PSFs. It is obvious that this is not the case in practice. Therefore, in a second set of experiments, we attempted the simulation of a real case

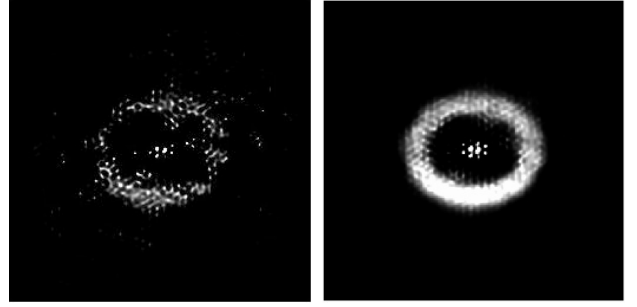


Fig. 6. Examples of reconstructions provided by OSEM when different PSFs are used for convolution and deconvolution. The PSFs used to convolve the object have $SR \approx 70\%$ while the PSFs used to deconvolve the images have $SR \approx 62\%$. To the *left*, the case where the integrated magnitude of the ring is 12.25 and to the *right* the case where it is 10.25.

using different sets of PSFs for convolving the object and deconvolving the images. To this purpose, we assumed the same orientations of the baseline considered in the previous set of experiments but we used AO-corrected PSFs with $SR \approx 70\%$ for convolution and AO-corrected PSFs with $SR \approx 62\%$ for deconvolution. These PSFs have been generated by the method described in Anconelli et al. (2005) and they simulate PSFs extracted from an off-line reference star.

The attempt of reconstructing the same object used in the first set of experiments was unsuccessful. Even if the two sets of PSFs are not very different, the difference between their values is too large with respect to the accuracy required in the reconstruction of such a hard astronomical object. The reconstruction of the ring looks completely erased both with OSEM and with the regularized algorithm. For this reason we modified the model by decreasing the integrated magnitude of the ring, while keeping fixed that of the binary, to reduce the gap between their fluxes. In particular we considered two cases: in the first, the integrated magnitude of the ring is 12.25 while, in the second, it is 10.25.

In Fig. 6 we show the reconstructions provided by OSEM. They do not correspond to the minimum of the rms error on the ring, since this is reached after a very small number of iterations (of the order of 10) so that the binary is not yet resolved. For instance, in the case of integrated magnitude 10.25, the minimum rms is 16%, while that of the reconstruction of Fig. 6 is about 19%. Anyway, the reconstruction obtained in the case of magnitude 12.25, does not allow an estimate of the parameter η while this is possible in the case of magnitude 10.25. We remark that, in this case, there is a factor 10^3 between the flux of the primary star and the maximum flux on the ring and that, if we deconvolve the images using the exact PSFs (inverse crime), then OSEM already provides an excellent reconstruction, so that the regularized algorithm is not needed. Indeed, after 1000 iterations, the reconstruction error of the ring is about 2% and also the reconstruction of the binary is very accurate. However, the regularized algorithm is required in the case of inexact knowledge of the PSFs, because, as we will show, it can improve the quality of the reconstruction.

As already mentioned, using PSFs with $SR \approx 62\%$ for deconvolution, OSEM provides a minimum reconstruction error of about 16% after 10 iterations, with an estimate of about 1.4×10^6 for the maximum value of the ring. Therefore we use a value of η greater than this one and precisely $\eta = 5 \times 10^6$. About the choice of μ , if we use the expected value of the functional $J(f, g)$ corresponding to the exact model (that is again of the order of 9.9×10^4), and the value of $J_R(f)$, that is now 2.9×10^{15} , we find a value of μ of the order of 3×10^{-11} . We checked by

numerical simulations that this value is too small and does not provide regularization of the ring.

This result is interesting. Indeed, we discovered that the value of μ is controlled by the value of $J(f, g)$ corresponding to the PSFs used for deconvolving the object. This value is much greater than the previous one and is of the order of 3.38×10^8 . It implies a value of μ of the order of 1.2×10^{-7} . By performing a rough search around this value, we obtained the best reconstruction with $\mu = 2.5 \times 10^{-7}$. The rms error on the ring has a typical semiconvergent behaviour and a minimum of 13.8% is reached after 10 iterations.

As a final experiment, we attempted an improvement of the result by means of the iterative blind deconvolution (IBD) method we recently implemented and tested (Desiderà et al. 2006). As a byproduct we have recognized that an improvement of this method may be convenient: it consists in introducing a constraint on the *SR* of the PSFs in the PSF boxes and it will be described in detail in forthcoming papers. Therefore we assumed to know the *SR* of the PSFs associated with the scientific object (about 70%).

The IBD method was initialized with the reconstruction of the ring provided by HDR and corresponding to the minimum reconstruction error and with the PSFs previously used for deconvolution (*SR* \approx 62%). We used 20 cycles of asymmetric IBD (1 iteration in the object box and 5 iterations in the PSFs boxes). The error on the ring increases, but this is not unexpected since IBD does not contain a regularized algorithm. However, the important point is that the PSFs are improved by IBD. Indeed, the rms error between the PSFs with *SR* \approx 70% and those with *SR* \approx 62% is about 11% while the rms error between the PSFs with *SR* \approx 70% and those at the exit of IBD is about 6%.

These PSFs are used in the HDR algorithm, with the value of η estimated above. About μ , we remark that the value of $J(f, g)$ corresponding to the new PSFs is now 1.15×10^8 , providing $\mu = 3.95 \times 10^{-8}$. A rough search around this value provided an optimal value that was again of the order of 2.5×10^{-7} . The rms error on the ring has now a nice convergent behaviour and an error of about 13.2% is reached after 100 iterations. The improvement is not spectacular but significant.

In Fig. 7 we show the level curves for the original object and the reconstructions obtained with the different methods. The level curves of the OSEM reconstruction correspond to that shown in Fig. 6 (right panel), while the level curves of the HDR reconstruction correspond to the result provided by 10 iterations, with a rms on the ring of about 14%. Since the number of iterations is small, the binary is not yet well resolved. To this purpose it should be necessary to use about 100 iterations, but then the rms on the ring increases to 15.5%. It is obvious that the main advantage of the reconstruction based on the PSFs obtained by means of IBD is that the rms has a convergent behaviour, so that it is possible to have a good reconstruction of the binary, without degrading the reconstruction of the ring.

The improvement in the reconstruction is confirmed by looking at the normalized residuals. All the residuals show now strong space correlations due to the fact that we do not know the correct PSFs. However these correlations are weaker in the case of the reconstruction obtained by means of the PSFs improved by IBD.

5. Concluding remarks

In this paper we propose a method for multiple image deconvolution in the case of images with high dynamic range. The method applies to scenes consisting of bright point objects and

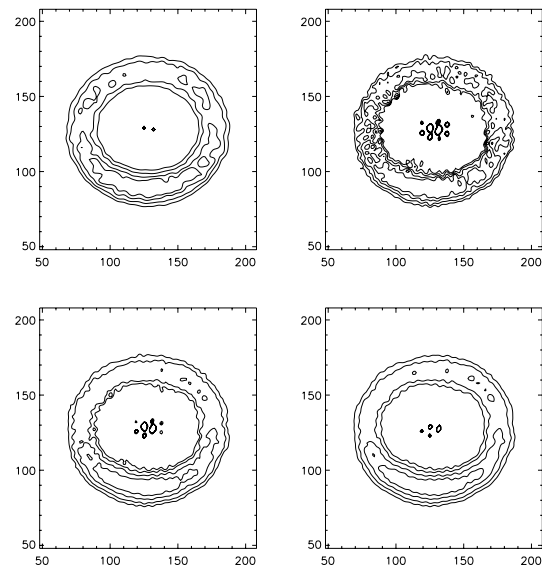


Fig. 7. Reconstructions of the level curves of the object with integrated magnitude of the ring 10.25. The values of the level curves are obtained from those of Fig. 1 by multiplying by a factor of 10^2 . Different PSFs for convolution and deconvolution are used (see the text). *Upper-left panel:* the object. *Upper-right panel:* the OSEM reconstruction shown in Fig. 6. *Lower-left panel:* the HDR reconstruction (the values of the parameters η and μ are indicated in the text). *Lower-right panel:* the HDR reconstruction obtained using the PSFs corrected by the blind method.

faint diffuse objects, that do not superimpose. It is an iterative method derived from a regularization of the Csiszàr I-divergence and consists in a simple modification of the multiple image RLM or of its accelerated version OSEM. The method has been tested on a difficult object derived from a model of young binary star and it is very effective in the case of accurate knowledge of the PSFs. If this condition is not satisfied, then reconstruction is still possible in the case of a smaller difference of magnitude between the binary and the surrounding ring.

Acknowledgements. We thank Rick Puetter for an accurate review of the paper and for suggesting several corrections and additions that, we believe, have greatly improved the quality of our paper.

References

- Anconelli, B., Bertero, M., Boccacci, P., et al. 2004, Proc. SPIE, 5491, 932
- Anconelli, B., Bertero, M., Boccacci, P., & Carbillet, M. 2005, A&A, 430, 731
- Anconelli, B., Bertero, M., Boccacci, P., Carbillet, M., & Lanteri, H. 2006a, A&A, 448, 1217
- Anconelli, B., Bertero, M., Boccacci, P., Carbillet, M., & Lanteri, H. 2006b, JCAM, to appear
- Bertero, M., & Boccacci, P. 1998, Introduction to Inverse Problems in Imaging (Bristol: IOP Publishing)
- Bertero, M., & Boccacci, P. 2000a, A&AS, 144, 181
- Bertero, M., & Boccacci, P. 2000b, A&AS, 147, 323
- Carbillet, M., Correia, S., Boccacci, P., & Bertero, M. 2002, A&A, 387, 744
- Correia, S., Carbillet, M., Boccacci, P., Bertero, M., & Fini, L. 2002, A&A, 387, 733
- Csiszàr, I. 1991, Ann. Stat., 19, 2032
- Desiderà, G., Anconelli, B., Bertero, M., Boccacci, P., & Carbillet, M. 2006, A&A, 452, 727
- Geman, S., & Mc Clure, D. 1987, Proc. 46th Session of the ICI, Bulletin of the ICI, 5
- Lanteri, H., Roche, M., Cuevas, O., & Aime, C. 2001, Signal Processing, 81, 945
- Lanteri, H., Roche, M., & Aime, C. 2002, Inverse Problems, 18, 1397
- Mighell, K. J. 1999, ApJ, 518, 380
- Puetter, R. C., Gosnell, T. R., & Yahil, A. 2005, ARA&A, 43, 139
- Snyder, D. L., Hammoud, A. M., & White, R. L. 1993, JOSA, A10, 1014
- Wood, K., Crosas, M., & Ghez, A. 1999, ApJ, 516, 335